Nano Select

RESEARCH ARTICLE OPEN ACCESS

Fabrication of Template-Assisted NanoMIPs: Nano-Sized Polymers for the Extraction of Ferulic Acid in Spiked Urine Sample

Aqil Faiz Mohamad Ramezan | Rachel Marcella Roland | Showkat Ahmad Bhawani | Muhammad Syafali Sabri | Aldrin Felix Simbas

Faculty of Resource Science and Technology, Universiti Malaysia Sarawak, Kota Samarahan, Sarawak, Malaysia

Correspondence: Rachel Marcella Roland (rrmarcella@unimas.my)

Received: 8 October 2025 | **Revised:** 18 January 2026 | **Accepted:** 7 April 2026

Keywords: adsorption | characterization | extraction | ferulic acid | microemulsion | molecular imprinted polymer

ABSTRACT

Ferulic acid (FA), a phenolic compound abundant in plant-based foods and traditional medicines, exhibits potent antioxidant, antidiabetic, and neuroprotective properties. However, extracting FA from natural and biological matrices remains challenging due to its susceptibility to oxidation and hydrolysis. While molecular imprinting polymer (MIP) technology offers selective extraction capabilities, existing approaches employ bulk-sized polymers with limited surface accessibility and slow binding kinetics. This study addressed these limitations by developing nano-sized molecularly imprinted polymers via oil-in-water microemulsion polymerization, employing methacrylic acid (functional monomer), ethylene glycol dimethacrylate (crosslinker), and benzoyl peroxide blend with dicyclohexyl phthalate (initiator). Comprehensive characterization using Brunauer–Emmett–Teller (BET) analysis, transmission electron microscopy (TEM), and Fourier-Transform infrared spectroscopy (FTIR) revealed that nano MIPs exhibited exceptional surface properties: specific surface area of 106.44 m^2/g with mean particle diameter of 42.72 nm, enabling rapid equilibrium binding within 30 min. Under optimized conditions (pH 7, 10 ppm FA, 0.1 g dosage), the nano MIP achieved 80.92% binding efficiency compared to 58.5% for controls, with validated recovery of 85.2% from spiked human urine samples. These results establish nano-scale MIPs as effective alternatives to conventional extraction methods for biological sample analysis and clinical applications.

1 | Introduction

Ferulic acid (FA), a hydroxycinnamic acid derivative, is widely distributed in plant-based matrices including fruits, vegetables, and grains, and represents one of the most prevalent phenolic compounds in nature [1]. Beyond its abundance, FA exhibits multifaceted therapeutic properties including antioxidant, antidiabetic, antihypertensive, anti-inflammatory, and neuroprotective effects, making it a compound of significant interest for pharmaceutical and nutraceutical applications [2]. Despite its therapeutic potential, FA extraction from natural and biological matrices remains challenging due to its chemical instability particularly susceptibility to oxidation and hydrolysis and the complexity of source matrices whether fruit, seed, leaf, or stem [3]. These limitations necessitate development of selective extraction methods capable of isolating FA while preserving its biological activity.

Molecular imprinting polymer (MIP) technology has emerged as a powerful approach for creating synthetic recognition materials that mimic biological receptors such as antibodies and enzymes [4]. MIPs are synthesized through formation of a stable template–monomer complex that yields recognition cavities with high affinity and exceptional specificity for target molecules [5]. Upon template removal, these imprinted sites become available for

selective rebinding with the target analyte from complex matrices. In analytical chemistry and environmental remediation, MIPs function as cost-effective, reusable alternatives to biological recognition elements, offering advantages in operational simplicity, thermal stability, and manufacturing reproducibility [6].

While molecular imprinting has proven effective for selective extraction of phenolic compounds, recent MIP-based approaches for FA detection and extraction have been limited in scope and application [1]. Previous studies have primarily focused on bulk-sized MIPs (particle size > 100 nm) or sensor applications employing nanostructured MIPs with limited surface characterization [7]. Key limitations in existing work include are large particle sizes resulting in slow mass transfer kinetics and extended equilibration times, insufficient characterization of critical surface properties (specific surface area, pore volume, pore size distribution) that determine the binding capacity, minimal application validation in complex biological matrices, and lack of systematic comparison between MIP performance and non-imprinted polymer (NIP) controls in real-world applications [8].

Nano-sized MIPs synthesized via microemulsion polymerization can potentially overcome these limitations by providing enhanced surface area-to-volume ratios enabling higher density of accessible binding sites, faster binding kinetics due to shortened diffusion pathways, and more defined pore architectures complementary to target molecule geometry [9]. Recent advances in MIP nanotechnology suggest that comprehensive characterization using Brunauer–Emmett–Teller (BET) analysis reveals the structural basis for superior adsorption performance, yet few studies have systematically integrated nano-scale synthesis with complete surface characterization and biological matrix validation for FA extraction.

Therefore, this study aimed to synthesize nano-sized FA-imprinted polymers via oil-in-water microemulsion polymerization using a rational polymer design, characterize their morphological and surface properties using transmission electron microscopy (TEM), scanning electron microscopy (SEM), Fourier-Transform infrared spectroscopy (FTIR), energy-dispersive x-ray spectroscopy (EDX), BET analysis, and thermogravimetric analysis (TGA) to establish structure–property relationships, optimize adsorption parameters (contact time, initial FA concentration, polymer dosage, pH) to identify operational conditions for maximum binding efficiency evaluate selectivity of imprinted sites relative to structurally similar competitor molecules and validate practical applicability in spiked human urine samples as a complex biological matrix [3]. This comprehensive approach allows for mechanistic understanding of the imprinting effect and enables rational optimization of MIPs for clinical and analytical applications.

2 | Results and Discussion

2.1 | Fourier Transform Infra-Red Spectroscopy (FTIR)

FTIR is the most prevalent application for identifying the functional groups in materials. It is used to find different functional groups in the range of 4000–400 cm^{-1} [10]. Figure 1 provides information about the various functional groups present in MIP and NIP.

The FTIR analysis was conducted to identify the chemical composition and the bonding characteristics of the synthesized MIP of FA and its NIP. The FTIR spectrum of MIP of FA would display peaks comparable to FA template molecule, MAA functional monomer and EGDMA cross-linker as shown in Figure 1. However, the FTIR spectrum of NIP only showed peaks corresponding to MAA functional monomer and EGDMA cross-linker.

Based on Figure 1, both MIP and NIP showed characteristic absorption bands at 2954.57 and 2921.35 cm^{-1}, respectively. This indicated the existence of a carboxylic OH group from methacrylic acid (MAA) that acts as a functional monomer in the MIP and NIP synthesis. The study had confirmed that in the case of pure acrylic species, the 3000 and 2600 cm^{-1} bands are related to the carboxyl OH groups which are hydrogen-bonded to other carboxyl groups, and in the case of aqueous solutions, these groups are hydrogen-bonded to water [11].

Both MIP and NIP exhibited strong carbonyl (C═O) stretching peaks at 1722.84 cm^{-1} (MIP) and 1722.81 cm^{-1} (NIP), confirming successful incorporation of MAA functional monomer and EGDMA crosslinker into the polymer matrix. The near-identical peak positions indicate that template presence during MIP synthesis does not significantly alter the fundamental chemical bonding environment of the polymer backbone [12].

Besides that, the FTIR spectra of both MIP and NIP showed medium peaks at 1452.86 and 1453.70 cm^{-1}, respectively. Small peaks also appeared at 1388.45 cm^{-1} of MIP and 1388.99 cm^{-1} of NIP. These peaks may be attributed to CH_2 bond bending and CH_3 bending of EGDMA as the cross-linker and MAA as the functional monomer.

The peaks at 1249.79 and 1249.40 cm^{-1} corresponded to C—O stretching from the ester groups present in the EGDMA cross-linker as shown in Figure 1. Moreover, the peaks of MIP and NIP at 1145.31 and 1145.86 cm^{-1}, respectively, may be associated with C—O—C stretching vibration. This is due to ester linkages within the EGDMA cross-linker or other oxygen-containing components of the synthesized MIP and NIP. Another medium peak at 958.13 and 960.71 cm^{-1} of MIP and NIP, respectively, were likely attributed to the C—H out-of-plane bending vibrations of trans-alkene groups (C═C—H), originating from unreacted double bonds in the MAA functional monomer or the formation of *trans* configurations within the polymer structure.

In addition, the peak appeared at 816.30 and 754.22 cm^{-1} suggested the presence of an aromatic ring with a specific substitution pattern, and these peaks corresponded to C—H out-of-plane bending vibrations of the aromatic hydrogens. However, a critical observation is the absence of distinguishable FA-specific aromatic C—H out-of-plane bending at 816.30 cm^{-1} in the MIP spectrum after template removal, suggesting complete FA elution during the washing process. This contrasts with incomplete template removal reported in some MIP studies, where aromatic peaks persist even after extensive washing [13]. The complete removal observed here validates the proper washing protocol confirms

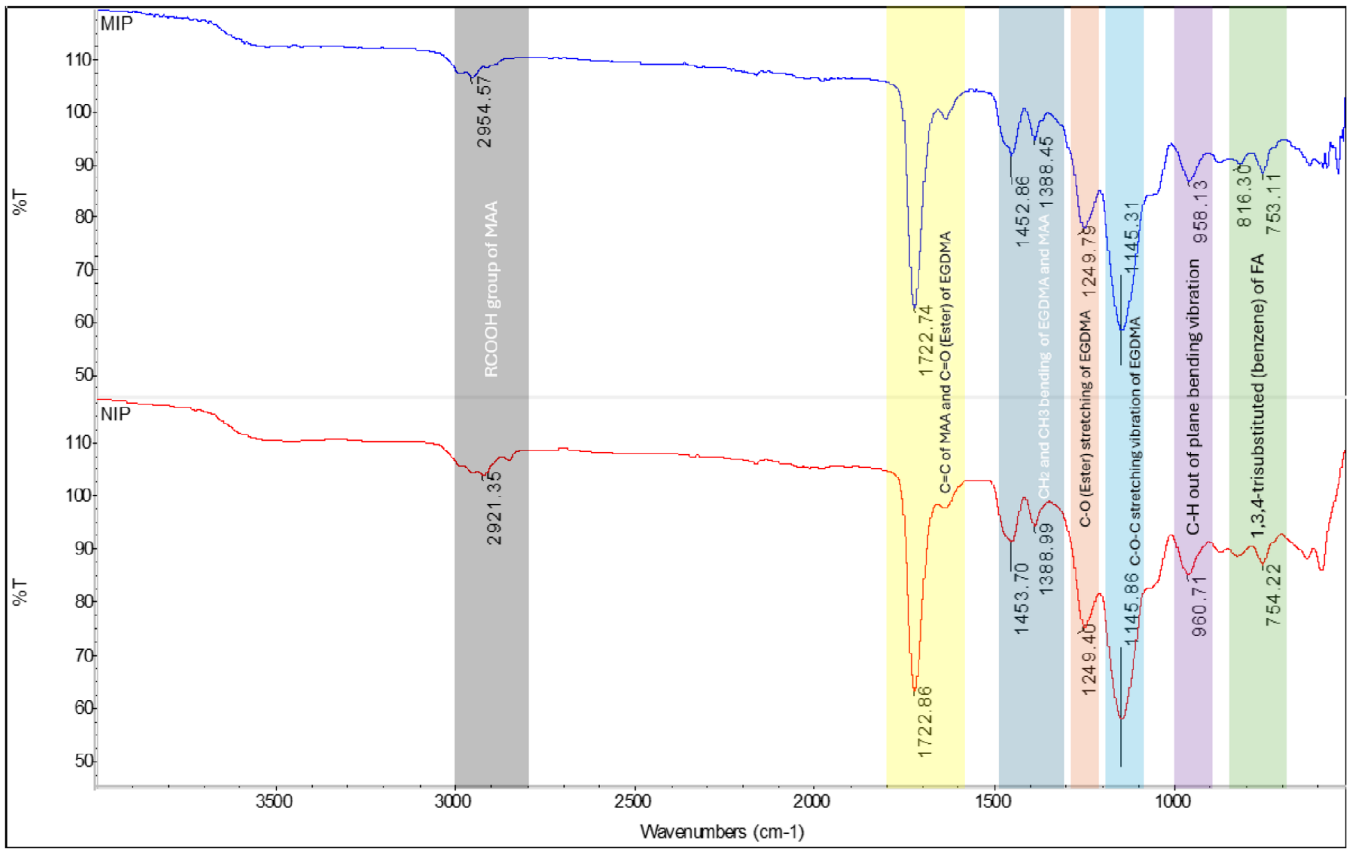

FIGURE 1 | IR spectra of MIP and NIP.

that binding sites are available for rebinding experiments, not occupied by residual template [14].

However, the peak at 754.22 cm^{-1} of NIP may be due to a different type of substitution or a combination of substitution patterns if there are minor impurities or variations in the aromatic environment. The peak at 753.11 cm^{-1} was also a characteristic of aromatic C—H out-of-plane bending vibrations. This may be due to the presence of an aromatic ring.

2.2 | Scanning Electron Microscopy (SEM)

Figure 2 depicts the SEM analysis of synthesized MIP and NIP showed the polymer surface morphology and structural characteristics at a very high resolution of 100k magnification. Both MIP of FA and NIP were irregular in shape and not uniform in size as shown in Figure 2. Besides that, the polymer particles of MIP and NIP were seen to be agglomerated. This may be due to the usage of EGDMA as the cross-linker that functions to control the morphology of synthesized polymers particles. The formation of MIP and its final size can be influenced by the choice of cross-linkers used during the preparation of MIP [9].

The mean diameter of MIP of FA and its NIP were 70.84 and 85.27 nm, respectively. This showed that MIP of FA had smaller mean diameter as compared to its NIP. This is due to the presence of FA as the template molecule during the synthesis of MIP. The particle sizes of the synthesized polymers are affected by the presence of template molecules during MIP polymerization reaction [15].

2.3 | Electron Dispersive x-Ray (EDX)

EDX analysis is applied to determine elemental composition in the synthesized polymer of MIP and NIP as shown in Figure 3. Based on the EDX analysis of MIP of FA in Figure 3a, it was confirmed that carbon and oxygen presence were 71.00% and 29.00%, respectively. Similarly, NIP also contained about 79.33% of carbon and 20.67% of oxygen.

Both synthesized polymers contained > 70 wt% carbon and ~20–29 wt% oxygen, confirming successful incorporation of MAA and EGDMA monomers into the polymer backbone. No contaminating elements (N, S, P, metals) were detected, indicating clean synthesis without reagent impurities or equipment contamination [4]. The high carbon content (71–79 wt%) indicates a robust C—C and C—O covalent backbone providing excellent chemical stability across pH 3–11, solvent resistance to organic solvents [10].

Both synthesized polymers were mainly composed of carbon and oxygen, showing the backbone of the polymer structure. Polymer particles containing significant carbon content are desirable for applications due to their high stability, mechanical strength and resistance to environmental factors [16].

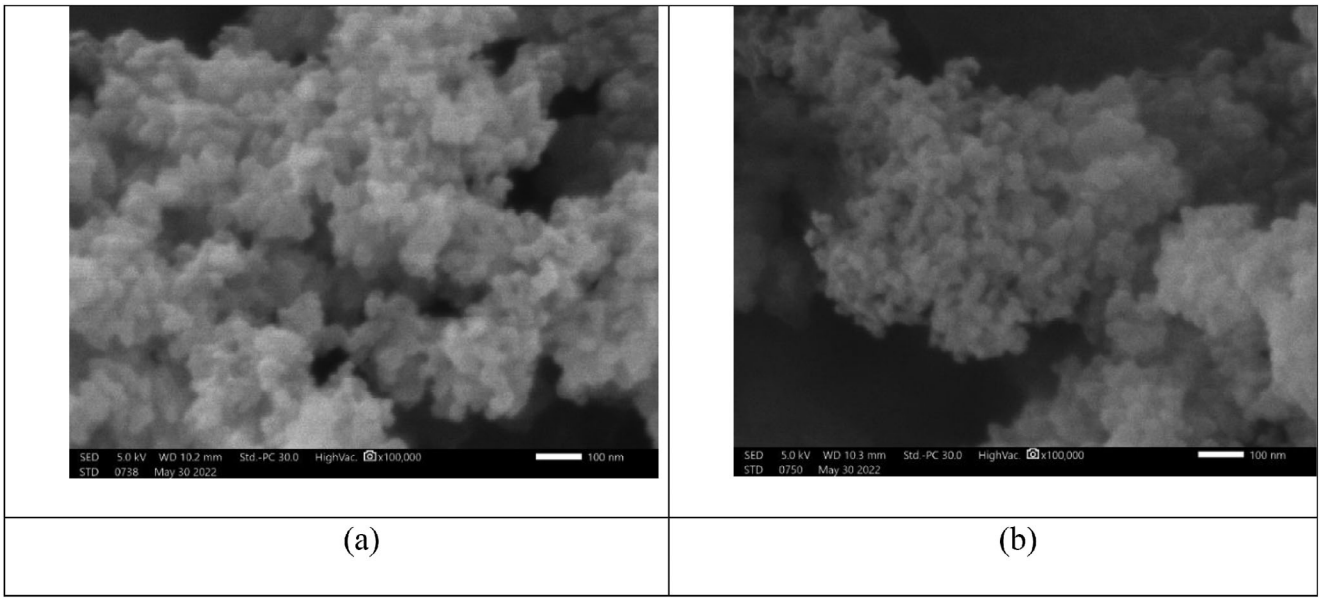

FIGURE 2 | SEM micrographs of (a) MIP and (b) NIP.

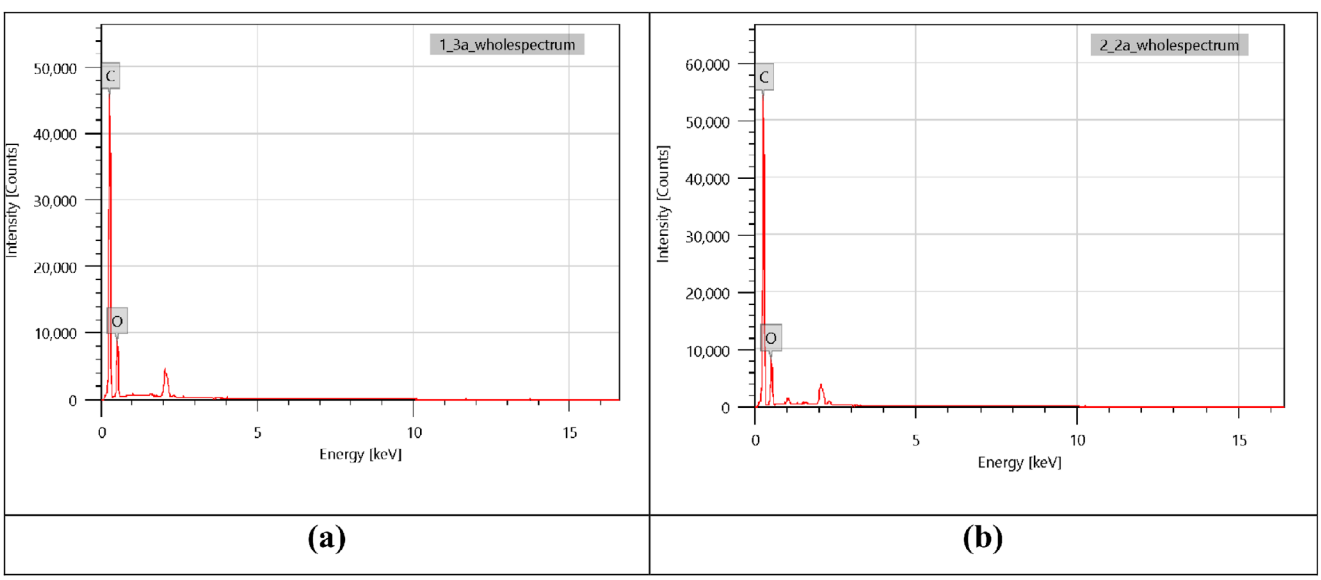

FIGURE 3 | EDX Sprectra of (a) MIP and (b) NIP from SEM.

2.4 | Transmission Electron Microscopy (TEM)

The morphological characteristics of the synthesized nano-MIP and NIP were evaluated using TEM at 100 000x magnification (Figure 4a,b). Analysis the MIP particles using Gatan DigitalMicrograph software revealed that the FA-imprinted polymers attained a predominantly spherical geometry with a mean primary particle diameter of 42.72 nm. In contrast, the NIP particles exhibited a significantly larger mean diameter of 83.17 nm, representing a 48.6% size reduction in the presence of the template molecule.

Critically, this secondary agglomeration (visible in dried TEM samples) must be distinguished from the primary particle size (42.72 nm for MIP, 83.17 nm for NIP), which represents authentic discrete nanoparticle dimensions. As solvent evaporates from the grid, capillary forces and van der Waals interactions reversibly pack nanoparticles together; this physical agglomeration does not represent permanent chemical bonding or cavity damage [17].

The marked morphological distinctions where the MIP displayed sphericity and narrower size distribution compared to the irregular, heterogeneous NIP suggest that the template (FA) influences the nucleation kinetics. In the MIP synthesis, the formation of template–monomer complexes may function as additional nucleation sites within the microemulsion droplets, leading to a higher density of smaller, more uniform nuclei [6]. Conversely, NIP synthesis proceeds without this molecular guidance, resulting in fewer, randomly distributed nucleation events and subsequent heterogeneous growth. While emulsion

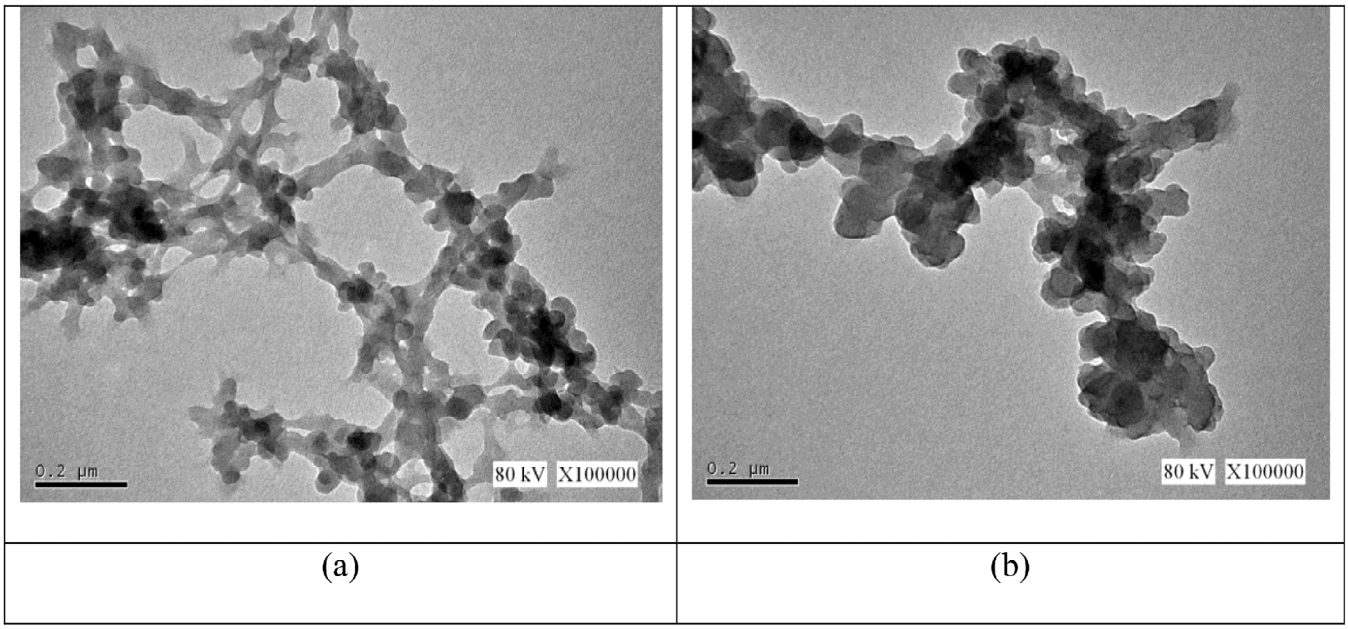

FIGURE 4 | TEM micrograph of (a) MIP and (b) NIP.

TABLE 1 | BET analysis of MIP and NIP of Ferulic Acid.

	MIP	NIP
Specific surface area (m^2/g)	106.44	5.35
Total pore volume (cm^3/g)	0.36	0.01
Average pore radius (Å)	136.28	70.61

polymerization typically yields globular particles, the integration of molecular imprinting here clearly refines the particle architecture, resulting in a high surface-area-to-volume ratio favorable for rapid mass transfer [12].

The 48.6% reduction in size for the MIP compared to the NIP further supports the rational design of the polymer. The presence of FA as a template organizes the functional monomers, potentially reducing the interfacial tension within the microemulsion droplets. This leads to a higher number of nucleation sites and, consequently, smaller and more uniform particles compared to the NIP, where nucleation is stochastic and less controlled.

2.5 | Brunauer–Emmett–Teller (BET) Analysis

Table 1 indicated the BET analysis that showed the specific surface area, average pore radius and total pore volume of MIP and NIP.

BET analysis revealed that MIP exhibits a 20-fold higher specific surface area (106.44 m^2/g) compared to NIP (5.35 m^2/g), accompanied by a 36-fold increase in total pore volume (0.36 cm^3/g vs. 0.01 cm^3/g) and nearly doubled average pore radius (136.28 Å vs. 70.61 Å). These dramatic differences mechanistically reflect the template-induced porosity formation central to molecular imprinting theory [18].

The higher surface area of the MIP indicates a greater accessible region for molecular recognition and binding with template molecules, as it offers more binding sites and enhances the selectivity of the MIP compared to the NIP [16]. Hence, MIP of FA indicates the successful imprinting and generating more specific binding sites for FA that eventually lead to higher binding efficiency.

The total pore volume of the MIP was calculated as 0.36 cm^3/g, while the NIP had a total pore volume of 0.01 cm^3/g. This showed that MIP had much larger total pore volume within its polymer due to higher volume available for FA template molecules to interact and bind within the polymer matrix as compared to that NIP. Larger total pore volume facilitates better binding of FA as the target molecules to polymer recognition sites and thus higher binding efficiency.

Based on Table 1, the average pore radius of both MIP and NIP were 136.28 and 70.61 Å, respectively. MIP of FA had greater average pore radius as compared to NIP. This clearly showed that MIP of FA had more defined pore size distribution around the FA template molecule, whereas NIP had broader and more random pore size distribution.

Thus, the formation of specific binding sites in the MIP matrix that are complementary to the FA template molecule will later enhance the MIP selectivity toward its target molecule. The addition of template molecules during MIP synthesis enhances the surface area, pore size and total pore volume relative to its NIP, thereby improving the polymer's binding efficiency for the target molecule [19, 20].

2.6 | Thermogravimetric Analysis (TGA)

TGA analysis is an important study in molecular imprinting since it was used to investigate the decomposition features of

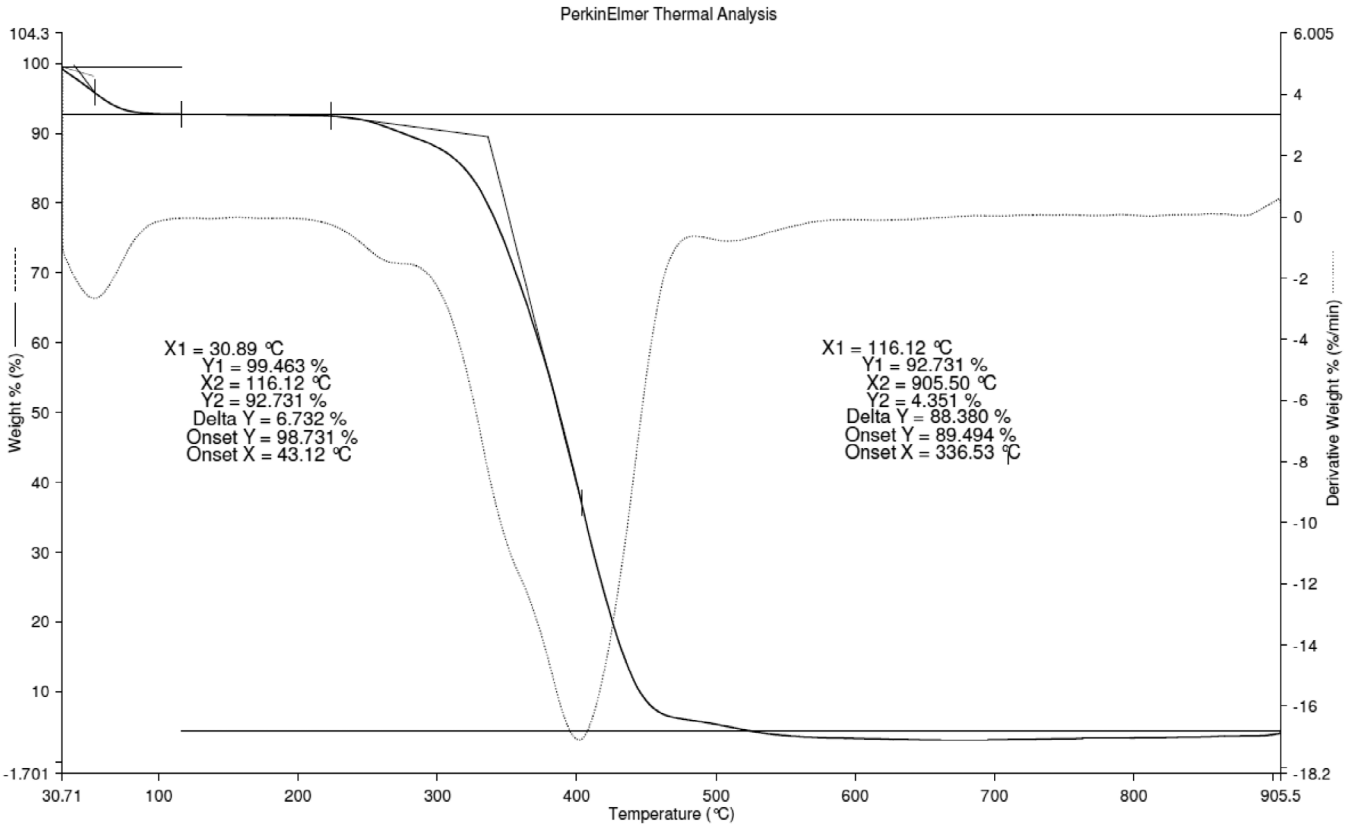

FIGURE 5 | Thermal Analysis of MIP FA.

the synthesized polymers [3]. MIP and NIP of FA were subjected to the TGA analysis in which the thermal degradation activity of both MIP of FA and its NIP were conducted from ~30°C to 900°C, in an atmosphere of nitrogen to determine the rate of the decomposition of each polymer in Figures 5 and 6.

Based on Figure 5, the first stage of weight loss was observed between 30.89°C and 116.12°C was due to the evaporation of moisture content and residual volatile solvents such as microemulsion mixture and methanol that entrapped within the porous polymer matrix.

The second stage weight loss of MIP of FA was detected between 250.0°C and 500.0°C, showing a significant and drastic decomposition with the MIP's weight reducing from 92.731% to 4.531% and hence, the calculated weight loss of MIP of FA was about 88.2%. This implied the thermal degradation of the main polymeric network of the MIP of FA. Notable decrease in weight loss is due to the decomposition MIP [21]. This drastic thermal decomposition of MIP of FA may be due to the breakdown of functional groups such CO, OH, CH_2, and CH_3 that were present in MAA functional monomer and EGDMA cross-linker. Besides that, the breaking of crosslinking within the rigid 3D polymer network causing the fragmentation of macromolecular chains may contribute to the drastic thermal decomposition of MIP of FA.

Figure 5 also showed the remaining mass of MIP of FA was ~4.531% at 905.50°C that was attributed to its thermal resistance. The remaining mass after TGA analysis of MIP of FA may be the nonvolatile residue left after a complete thermal degradation of organic components.

Figure 6 showed the thermal analysis of NIP in which the first stage of weight loss of NIP was observed at 30.20°C–130.58°C with 2.89% of weight loss. This weight loss is due to evaporation of moisture content such as water as well as residual volatile solvents such as microemulsion mixture and methanol from the polymer matrix.

The thermal degradation of NIP (Figure 6) was different in comparison with the thermal degradation of MIP of FA (Figure 5) because the thermal degradation of NIP occurred at two stages, initial thermal decomposition and drastic thermal decomposition. The second stage of weight loss of NIP occurred from 130.58°C to 298.82°C with a weight loss of 86.283%. This indicated the initial thermal decomposition of the functional group including CO, OH, CH_2, and CH_3 that were present in MAA functional monomer and EGDMA cross-linker within the NIP's polymer backbone. Then, the third stage of weight loss of NIP occurred at 298.82°C–450.0°C with a drastic decomposition from 86.283% of weight to 17.679% of weight.

This showed the complete thermal degradation of the cross-linked NIP backbone. EGDMA cross-linker is function to form a robust and three-dimensional network of a polymer, however, at the temperatures between 298.82°C and 901.36°C, the strong covalent bond within EGDMA cross-linker and the NIP chain are broken and eventually leading to the fragmentation of macromolecular chains.

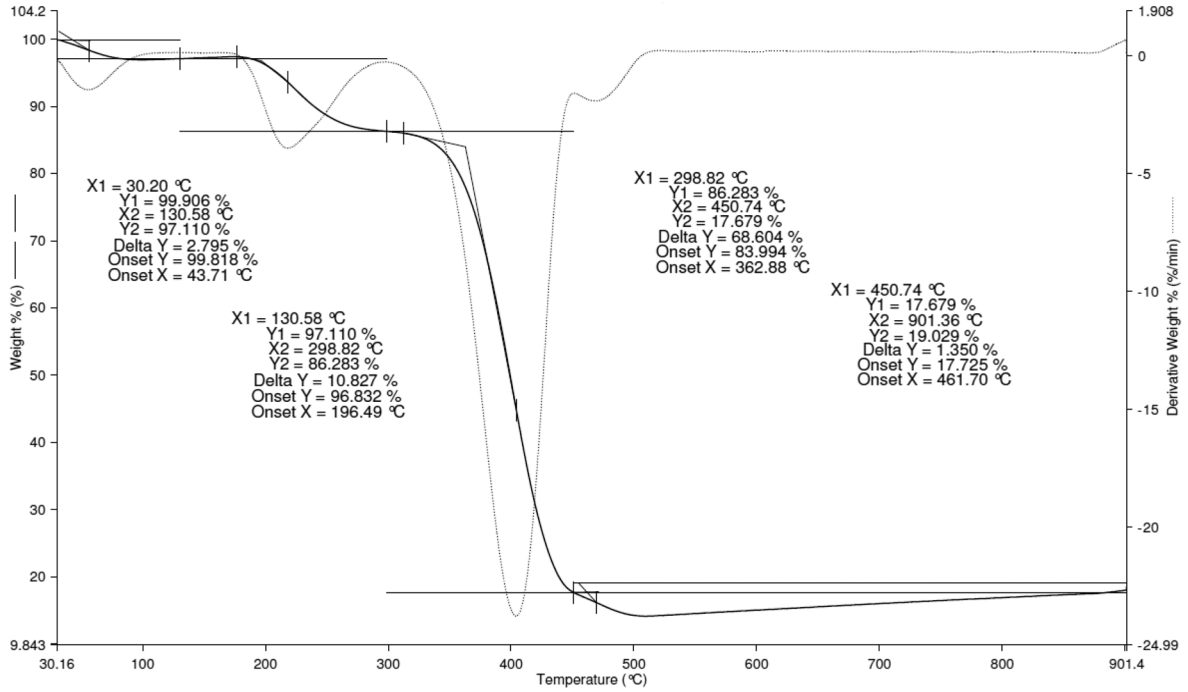

FIGURE 6 | Thermal Analysis of NIP FA.

At 901.36°C, the remaining mass of NIP left was ~ 17.679% of its original weight as shown in Figure 6. This is due to the nonvolatile residue left after a complete thermal degradation of organic components.

This difference can be attributed to the MIP resulting from organized polymerization around template molecules. In NIP, without template guidance, the polymer network forms heterogeneous regions with varying cross-link densities, leading to sequential thermal degradation [22]. The lower residual mass in MIP (4.531% vs. 17.679% for NIP at > 900°C) suggests more complete organic decomposition, indicating a purer polymer structure with fewer inorganic impurities or incompletely polymerized oligomers [12].

The higher thermal stability observed in the initial stages for MIP may indicate stronger intermolecular interactions within the imprinted network. This enhanced thermal stability is advantageous for practical applications requiring repeated use or exposure to elevated temperatures during sample processing [23].

2.7 | Batch Binding

Batch binding experiments of MIP of FA and its NIP were carried out to investigate the rebinding capacity of the synthesized polymers. Batch binding experiments were carried out. Also, the batch binding curves show that both MIP and NIP systems follow typical adsorption kinetics patterns, with rapid initial binding followed by equilibrium plateau formation [24]. Throughout these experiments, MIP–FA and NIP–FA samples were gathered at regular intervals of 5 min for the first 30 min and then 30-min intervals for the next 90 min. Then, the binding efficiency of those samples analyzed by using UV–vis Spectroscopy.

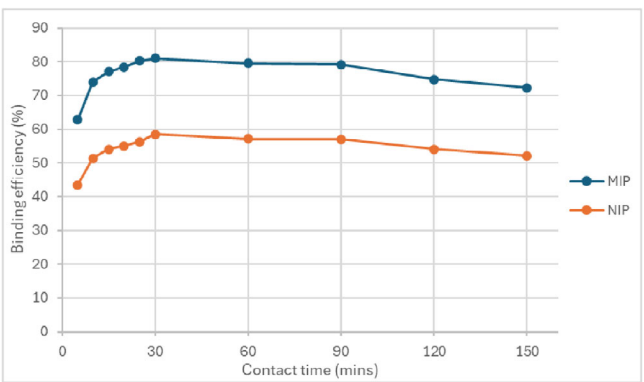

FIGURE 7 | Rebinding efficiency of MIP FA.

Based on Figure 7, the binding efficiency of MIP of FA increased from 0 to 30 min and then gradually decreased from 60 to 150 min. The initial rapid phase corresponds to binding at high-affinity recognition sites created during the imprinting process, while the slower phase represents interaction with lower-affinity sites and nonspecific binding [6]. The highest binding efficiency of MIP of FA was 80.92% that was obtained at contact time of 30 min. This depicted 30 min of contact time as the optimal time for rebinding process of MIP of FA. At this point, MIP FA fully engage with FA molecules, reaching adsorption–desorption equilibrium all high-affinity binding cavities are occupied, and further incubation does not increase FA uptake. This is because the rebinding of MIP with its template molecule was completed, and the adsorption process between MIP and its template molecule had reached equilibrium [25]. Beyond this timeframe, the binding efficiency slightly decreases, likely due to molecular rearrangement or competitive binding effects [26].

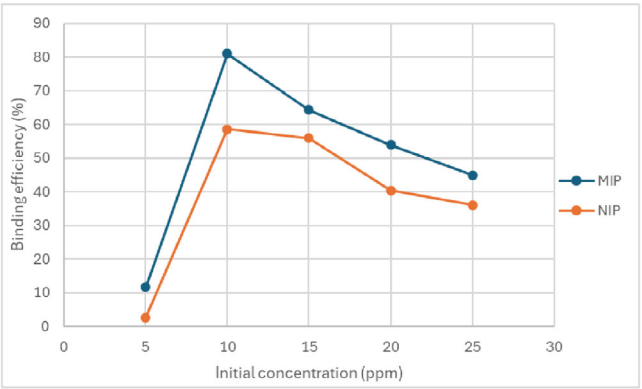

FIGURE 8 | Binding efficiency of MIP FA at different initial concentration.

FA-MIP binding reaches equilibrium within 30 min, with 80.92% of FA removed from 10 ppm solution. This rapid equilibration is mechanistically explained by the favorable mass transfer properties conferred by nano-scale particle size (42.72 nm) and high porosity (136.28 Å average pore radius).

Further increase in contact time of MIP rebinding with FA template molecules causes the binding efficiency of MIP to be decreased gradually as shown in Figure 7. This is because there were no empty binding sites as all binding sites in the MIPs had fully bound with the FA template molecules. After saturation point, no MIP rebinding with template or a slight reduction in the polymer's rebinding efficiency, as all available binding sites within the polymer matrix had already been saturated with its template molecule [25].

Figure 7 also showed the binding efficiency of NIP that had a similar pattern as MIP but with much lower binding efficiency. In comparison, MIP of FA had much higher binding efficiency as compared to its NIP with binding efficiencies of 80.92% and 58.5%, respectively. The specific surface area of the MIP is higher than that of the NIP, alone may increase the template binding [27]. The binding efficiency of the NIP rose between 0 and 30 min, then gradually declined from 60 to 150 min. The NIP had achieved its highest binding efficiency of 58.5% at a contact time of 30 min. This showed that NIP had much lower binding efficiency than MIP due to no presence of FA template molecules during the synthesis of NIP to generate specific binding sites for FA in the NIP cavity. NIP has a lack of specific binding sites for the binding with template molecules that leads to lower binding efficiency [12].

2.8 | Adsorption Studies

2.8.1 | Initial Concentration

Various initial concentrations of FA solutions including 5, 10, 15, 20, and 25 ppm were used to evaluate the influence of different initial concentrations of FA toward the MIP binding efficiencies. Figure 8 illustrated the comparison of adsorption efficiencies between MIP of FA and its NIP at various initial concentrations of FA solution (template molecule). The adsorption efficiencies of MIP toward FA increased from 5 to 10 ppm, then decreased until 25 ppm.

The adsorption capacities of MIP at different initial concentrations of 5, 10, 15, 20, and 25 ppm FA solution were 11.66%, 80.92%, 64.31%, 53.85%, and 44.9 %, respectively. As the initial concentration of FA increased, the adsorption capacity of the MIP also rose until it reached saturation at 10 ppm. So, the highest adsorption capacity of MIP was calculated at 80.92% at initial concentration of 10 ppm. The observed increase in FA adsorption efficiency by MIP from 5 to 10 ppm suggests that numerous binding sites were available within the MIP cavities to interact with the FA template molecules. The synthesized polymers have reached their peak for the binding of MIPs binding sites with the target molecule at this point [12]. Thus, 10 ppm of FA solution is the ideal initial concentration for the highest adsorption capacity of the synthesized MIP. Most high-affinity cavities are now filled, giving maximum capacity with still-strong selectivity [28].

However, further increase in initial concentrations of FA solution (15, 20, and 25 ppm) leads to decrease in the adsorption capacity of MIP. This could be because the matching binding sites of the FA template had taken up all the free binding sites in the polymers. Beyond the adsorption saturation point, any further increase in the initial concentration of template solution leads to the accumulation of template molecules around the MIP binding sites, which can obstruct efficient adsorption within the MIP cavities and consequently reduce the overall adsorption efficiency [25].

In comparison, the adsorption capacity of NIP had a similar trend to the MIP but with much lower adsorption efficiency. The adsorption capacities of NIP at different initial concentrations of 5, 10, 15, 20, and 25 ppm FA solutions were 2.67%, 58.5%, 55.93%, 40.34%, and 36.00%, respectively. This is because NIP lacks specific binding sites in its cavities that facilitate efficient adsorption of the template molecule, as its nonspecific binding sites do not match or correspond to its template molecule [27].

2.8.2 | pH

To determine the optimal pH for binding efficiency of MIP toward FA, the adsorption MIP-FA were tested with five different pH which is acidic (pH 1 and pH 3), neutral (pH 7), and alkaline (pH 11 and pH 13). pH test is an important test for MIP because pH can affect the dissociation status of both target compounds and MIP. Through the test, the other parameters are constant like initial concentration, contact time, and temperature [29].

In this study, several pH conditions of FA solutions were adjusted to acidic (pH 1 and pH 3), neutral (pH 7), and alkaline (pH 11 and pH 13). Figure 9 displayed the binding efficiency of MIP at pH 1, pH 3, pH 7, pH 11, and pH 13 were 3.85%, 13.14%, 80.92%, 5.68%, and 4.74%, respectively. Therefore, the optimal pH for the MIP to obtain the highest binding efficiency is at pH 7 (neutral condition).

The graph shows the binding efficiency of MIP against pH. The optimal pH for the MIP to rebinding with FA is pH 7 which

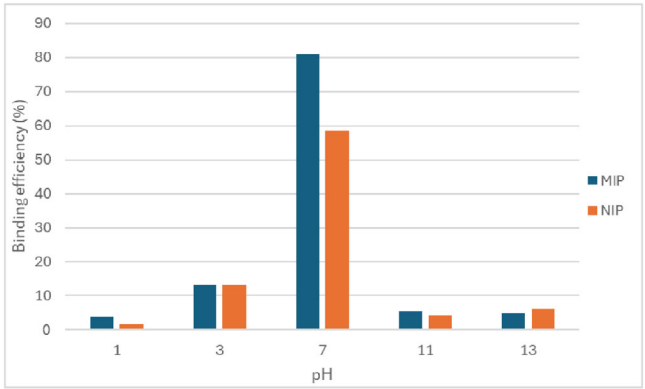

FIGURE 9 | Binding efficiency of MIP FA at different pH of FA solution.

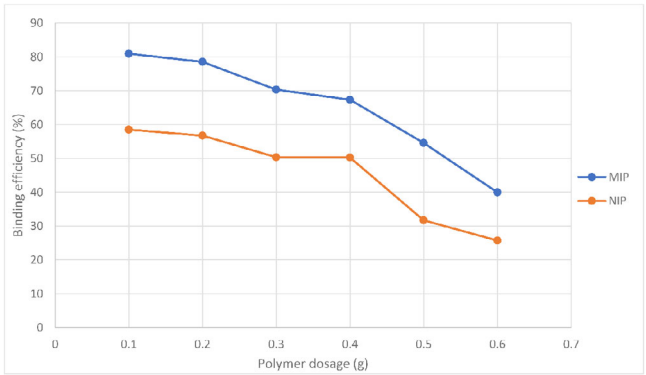

FIGURE 10 | Binding efficiency of MIP Fa using of different polymer dosage.

is 80.92% of binding rate. The pH 7 is the initial pH of the solution without modification. The physiological pH optimum (pH 7) is particularly significant for biological applications, as this represents the pH environment where FA would naturally interact with biological macromolecules [30].

Although the primary application of this work focuses on FA extraction from human urine (physiological pH 5.5–7.0), a comprehensive pH screening (pH 1–13) was performed to provide a complete ionization profile of both FA and polymer functional groups, enabling mechanistic understanding of binding interactions, assess MIP robustness and stability across a wide pH range, establish a foundation for future applications of this MIP system in environmental remediation and alternative matrices [15].

At pH 11 and pH 13, the binding efficiency of MIP is too low at 5.68%±0.17% and 4.74%±0.14%, respectively. MIP's functional groups become deprotonated, resulting negative charges on FA and the polymer backbone also generate electrostatic repulsion, leaving only weak nonspecific electrostatic attraction and minimal hydrophobic interactions to drive adsorption. Due to the high pH the adsorption was mostly attributed to electrostatic attraction, with very little contribution from other interactions like hydrophobic interaction and hydrogen binding [29].

At pH 1 and pH 3, the binding efficiency is lower than pH 7. The acidic conditions can protonate amino or other basic functional groups within the MIP cavities, altering the complementary binding environment originally designed for FA recognition. It is due to at low pH, functional group of MIP or template may be protonated, altering the interactions between the molecule and active MIP binding sites [25]. In acidic pH, the lower adsorption proved that the H^+ ion can be considered as competitor of template since the nitrogen in pyridine group in the MIP which is responsible for binding site of template are predominantly protonated [31].

2.8.3 | Polymer Dosage

In Figure 10, different polymers which are MIP will be used for adsorption FA. So, the polymer dosage that has been used are 0.1, 0.2, 0.3, 0.4, 0.5, and 0.6 g. This study is used to determine the optimal amount polymer been used to adsorb with highest efficiency. The parameters like pH, initial concentration of FA, time and temperature are constant.

The highest binding efficiency of FA is at polymer dosage 0.1 g with 80.92%±1.05% adsorption of FA. This shows that 0.1 g is the optimal dosage for binding. At 0.1 g, the polymer provides an optimal ratio of accessible binding sites to FA concentration, whereas higher dosages lead to underutilized cavities. Adsorption sites were occupied, the movement of template into the pore surface faster due to many binding sites were available and this continued until equilibrium was achieved [32].

While for the 0.2 g till 0.6 g of polymer dosage, the binding efficiency keeps decreasing. From 0.2 to 0.6 g, polymer particle aggregation reduces the number of accessible binding sites, causing a continuous decline in binding efficiency. With the increase in dosage amount, the polymer particles formed aggregates and due to this aggregation, the number of available binding sites accessible to template molecules have decreased [33].

Due to an excess of MIP particles, which encourage polymer particle aggregation and obstruct the binding process with the template molecule, an excessive polymer dose reduces adsorption effectiveness [5].

2.9 | Selectivity

This study involves competitive molecule which riboflavin because it has same characteristic and structure with FA. The purpose of this study is to determine the binding efficiencies of MIPs and NIPs toward molecules [5].

The Table 2 shows that distribution ratio of MIP in FA is higher than distribution ratio of MIP in riboflavin which is 16.85 mLg^{-1} for FA and 4.60 mLg^{-1} for riboflavin. The absorption partition coefficient K_D of template was much higher than that for adsorption of competitor molecules onto the adsorbent, demonstrating that the absorption ability of the template was much higher than that for competitor [34].

The relative selectivity coefficient for MIP FA is 1.12. This shows that the MIP are more selective toward FA rather than riboflavin. The higher distribution ratio of template is also since MIP can

TABLE 2 | Result of Selectivity Test on MIP between FA and Riboflavin.

Template	K_D of MIP (mLg^{-1})	K_D of NIP (mLg^{-1})	K^{sel}	k'
Ferulic acid (template molecule)	16.85	5.53	3.04	1.12
Riboflavin (competitive molecule)	4.60	1.69	2.72	

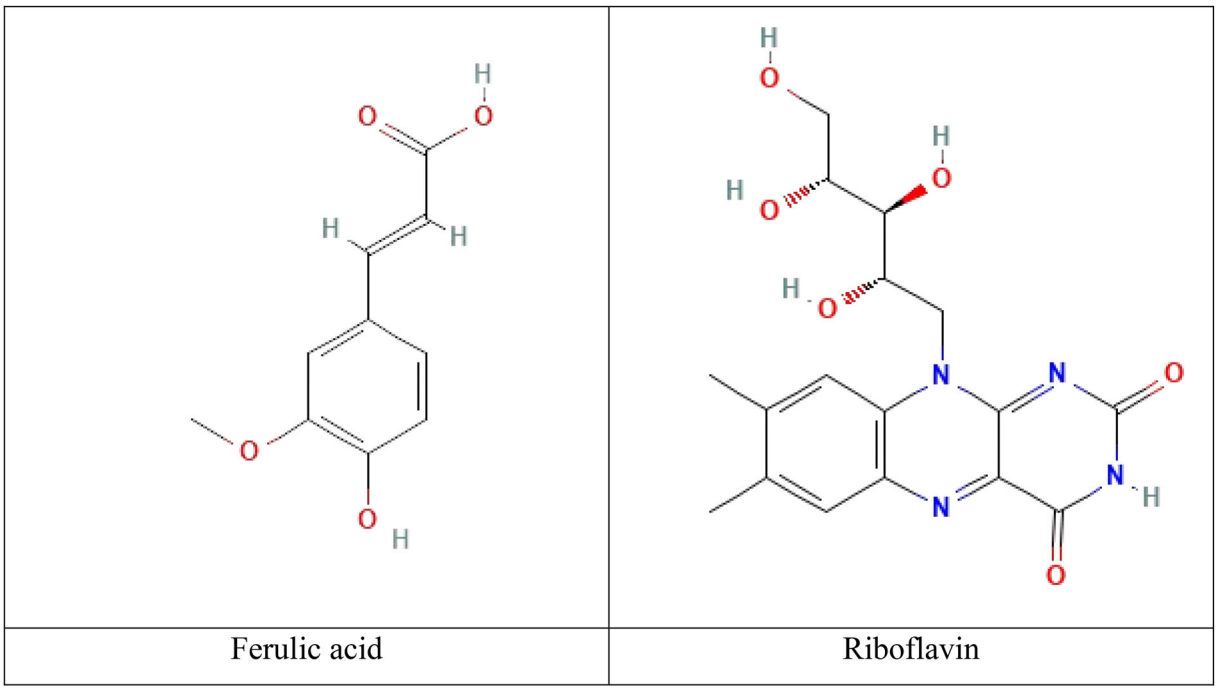

FIGURE 11 | Chemical structure of FA (template molecule) and Riboflavin (competitive compound).

recognize and attach the template molecules by specific binding sites that have been preserved as a memory [5].

The effectiveness of polymers to recognize selectivity is said to be influenced by characteristics such as material particle size and recognition site shape [25]. Also, the MIP's pores are unmatched with the competitor molecule in the size, shape, and spatial arrangement of the action sites, the competitor molecule are difficult to enter into these pores or these imprinted pores, and for these pores it is difficult to accept and bind the competitor molecule, leading to the very low binding capacity of the adsorbent particles for competitor molecule [24].

The modest relative selectivity coefficient ($k' = 1.12$) indicates that while MIP shows preferential binding for FA over riboflavin [35]. This can be explained by structural similarities both FA and riboflavin contain aromatic systems and hydrogen bonding moieties as shown in Figure 11. However, FA (MW 194 g/mol) differs significantly from riboflavin (MW 376 g/mol) in size and three-dimensional structure [33]. The imprinted cavities, templated by FA's specific dimensions and functional group arrangement (4-hydroxy-3-methoxycinnamic acid structure), provide better complementarity for FA than the larger, more complex riboflavin structure [35]. The template-imprinted cavities exhibit geometric and chemical complementarity to FA, ensuring binding affinity and selectivity unmatched by nonspecific rivals [3].

2.10 | Adsorption Isotherm

The adsorption kinetics of FA onto molecularly imprinted polymer (MIP-FA) were elucidated by fitting experimental data to both Pseudo-first-order (PFO) and pseudo-second-order (PSO) kinetic models as shown Figures 12 and 13. Model selection was based on rigorous statistical comparison including correlation coefficient (R^2), agreement between calculated and experimental equilibrium capacity, and error analysis functions.

Statistical analysis revealed that the PSO model provides superior fit across all criteria. The PFO model yielded $q_e = 0.00891$ mg/g, representing only 1.1% of the experimental q_e, a severe deviation demonstrating mechanistic incompatibility. PSO model yielded $q_e = 0.816$ mg/g, showing excellent agreement with experimental value. Additional statistical criteria confirm PSO superiority, $R^2 = 0.9986$ versus 0.9506. These results definitively establish PSO as the appropriate kinetic model [34].

So, the PSO kinetic model was the best-fitted kinetic model for MIP (FA) which the kinetic reaction was more inclined toward chemisorption, indicating that the FA molecule and the MIP (FA). The result indicates that the adsorption process of template on the MIP was dominated by chemical sorption and the adsorption capacity was proportional to the number of cavities on the MIP [36]. Moreover, this PSO kinetic model

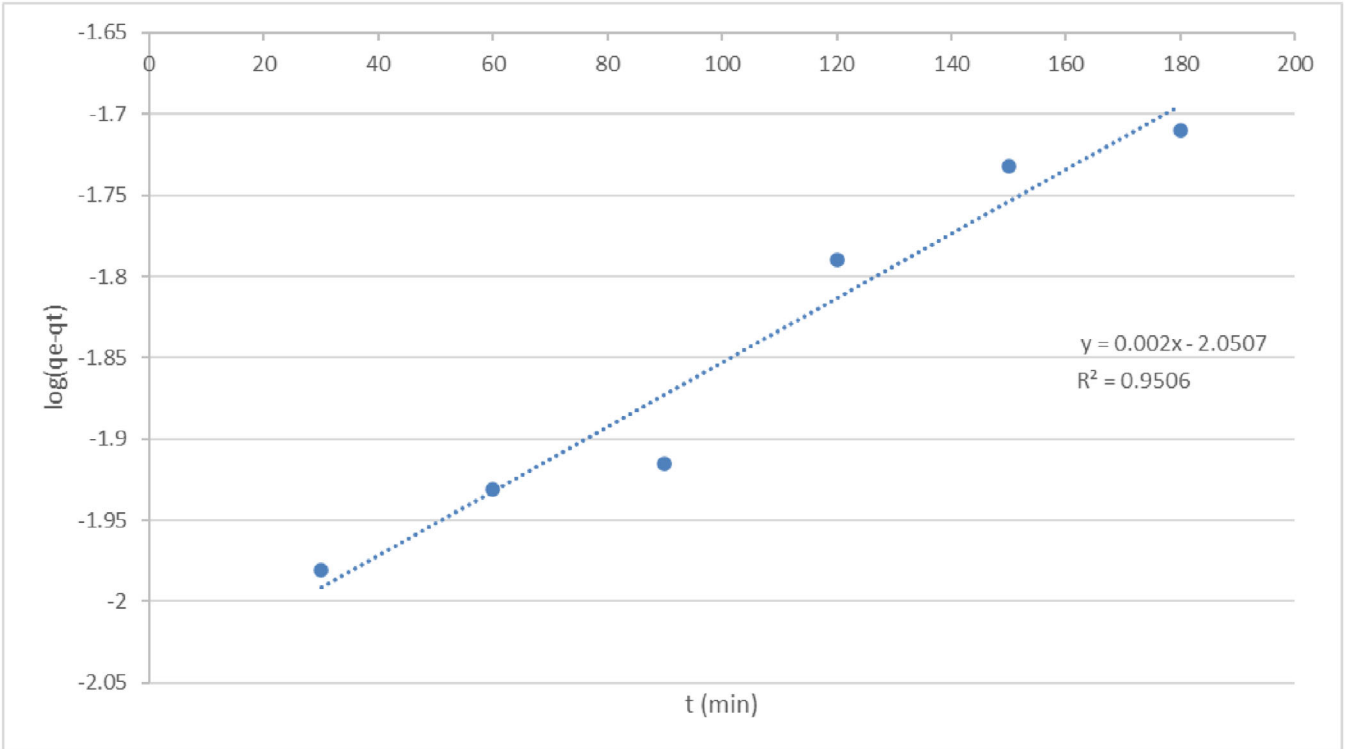

FIGURE 12 | The Pseudo first-order of MIP FA.

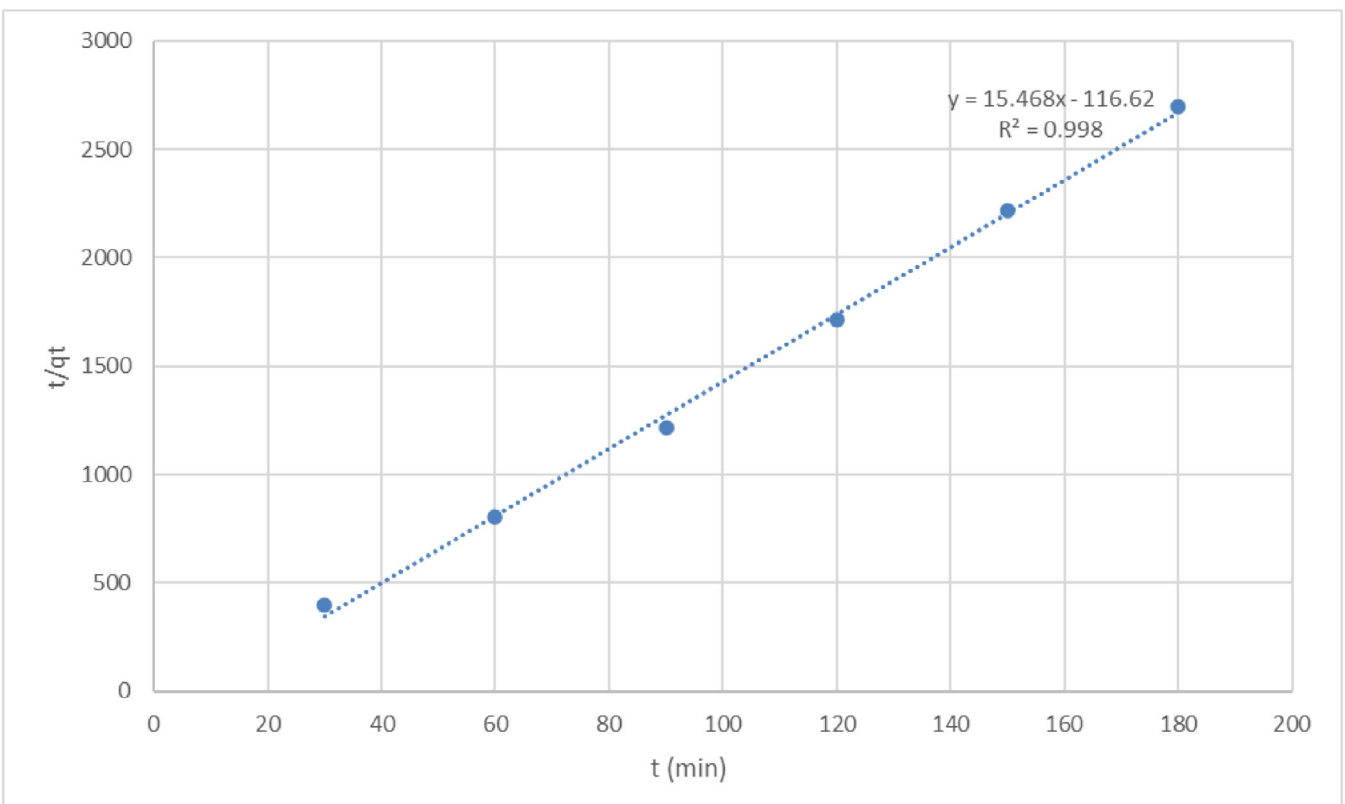

FIGURE 13 | The Pseudo second-order of MIP FA.

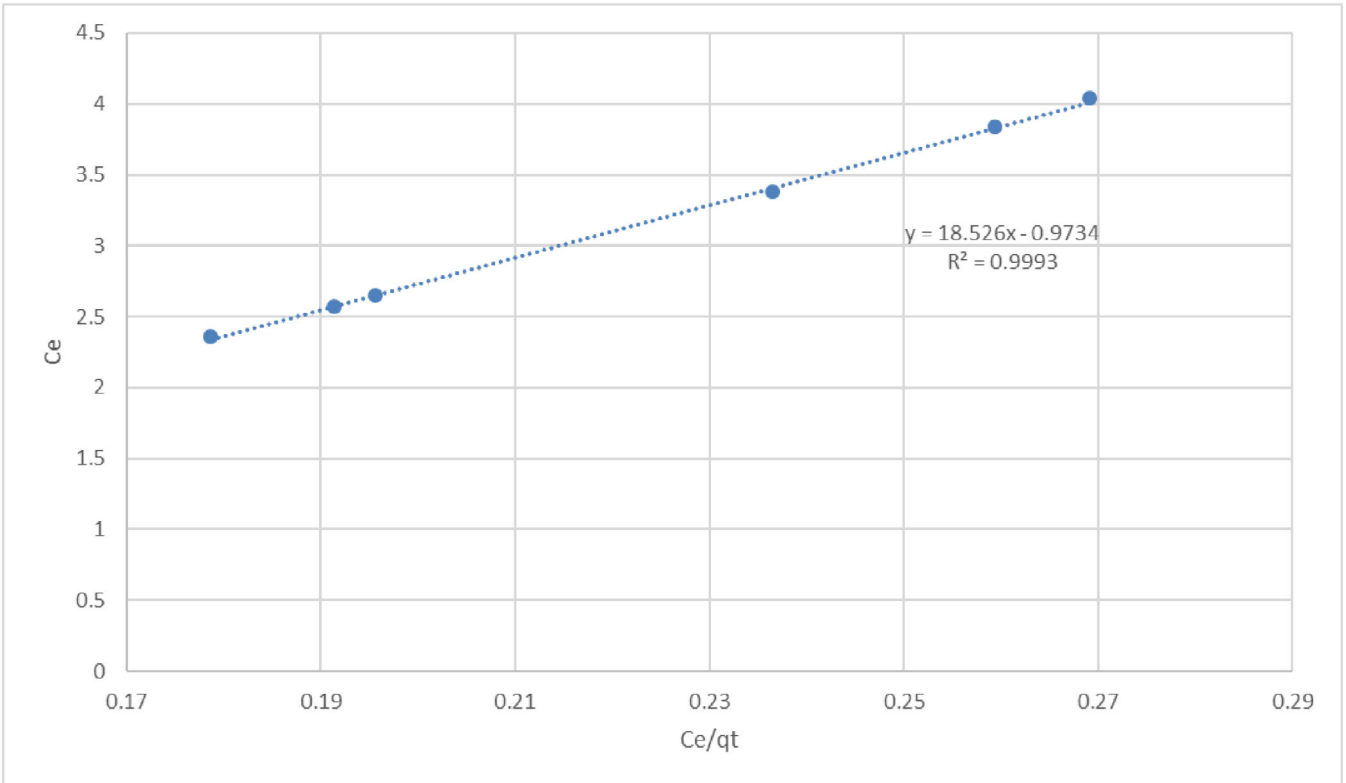

FIGURE 14 | Langmuir isotherm of MIP FA.

also indicated that the adsorption rate of solute is proportional to the available binding sites on the MIP as the adsorbent [37].

PSO kinetic parameters: k_2 = 0.0020 g/mg·min, q_e, cal = 0.816 mg/g, R^2 = 0.9986, initial sorption rate (h) = 0.00134 mg/(g·min). The PSO model definitively describes FA adsorption onto MIP-FA, supported by superior statistical fit across all criteria, mechanistic consistency with observed chemisorption via hydrogen bonding and molecular recognition, and physical validity [4]. This understanding reveals that FA adsorption is rate-limited by chemical reactions at template-imprinted cavities, making MIP-FA an excellent sorbent for selective FA extraction [36].

2.11 | Kinetic Isotherm

Two adsorption isotherm models which are Langmuir and Freundlich isotherms were applied to evaluate the mechanism of adsorption by MIP FA shown in Figures 14 and 15 and Table 3.

The slopes and intercepts of the plots were applied for the calculations of isotherm factors such as q_{max}, KL, RL, n, 1/n, and R^2 values as displayed in Table 4.

Generally, the Langmuir adsorption isotherm is defined as monolayer adsorption of adsorbate FA by MIP while the Freundlich adsorption isotherm is defined as multi-layer adsorption of adsorbate FA by MIP.

The experimental data fitting to the Langmuir isotherm model is based on several key assumptions which are a finite number of adsorption sites are uniformly distributed across the surface of the adsorbent, and each site has an equal affinity for the adsorbate, the adsorption process is reversible, adsorption occurs in a monolayer, meaning that once an adsorbate molecule occupies a site, no additional adsorption can take place at that location and there are no interactions between adsorbed molecules on adjacent sites [38].

Additionally, mono-layer sorption onto the adsorbent's surface and in its pores can be represented using the Langmuir model. This can demonstrate that diffusion is the rate-determining step and that the equilibrium results are well described by the Langmuir isotherm [39].

The R_L value is important to determine the type of adsorption isotherm, whether the adsorption is favorable ($0 < R_L < 1$), unfavorable ($R_L > 1$), or irreversible ($R_L = 1$) [40]. Besides that, the R_L value was 0.0531, suggesting favorable adsorption of FA by MIP-FA as shown in Table 4.

2.12 | Application

Human urine represents a challenging biological matrix for analytical extractions due to its inherent chemical complexity and compositional variability. A typical fresh urine sample contains > 3000 different chemical compounds, including proteins (albumin, globulins), electrolytes (sodium, potassium, chloride, phosphate, sulfate), organic acids (creatinine, uric acid,

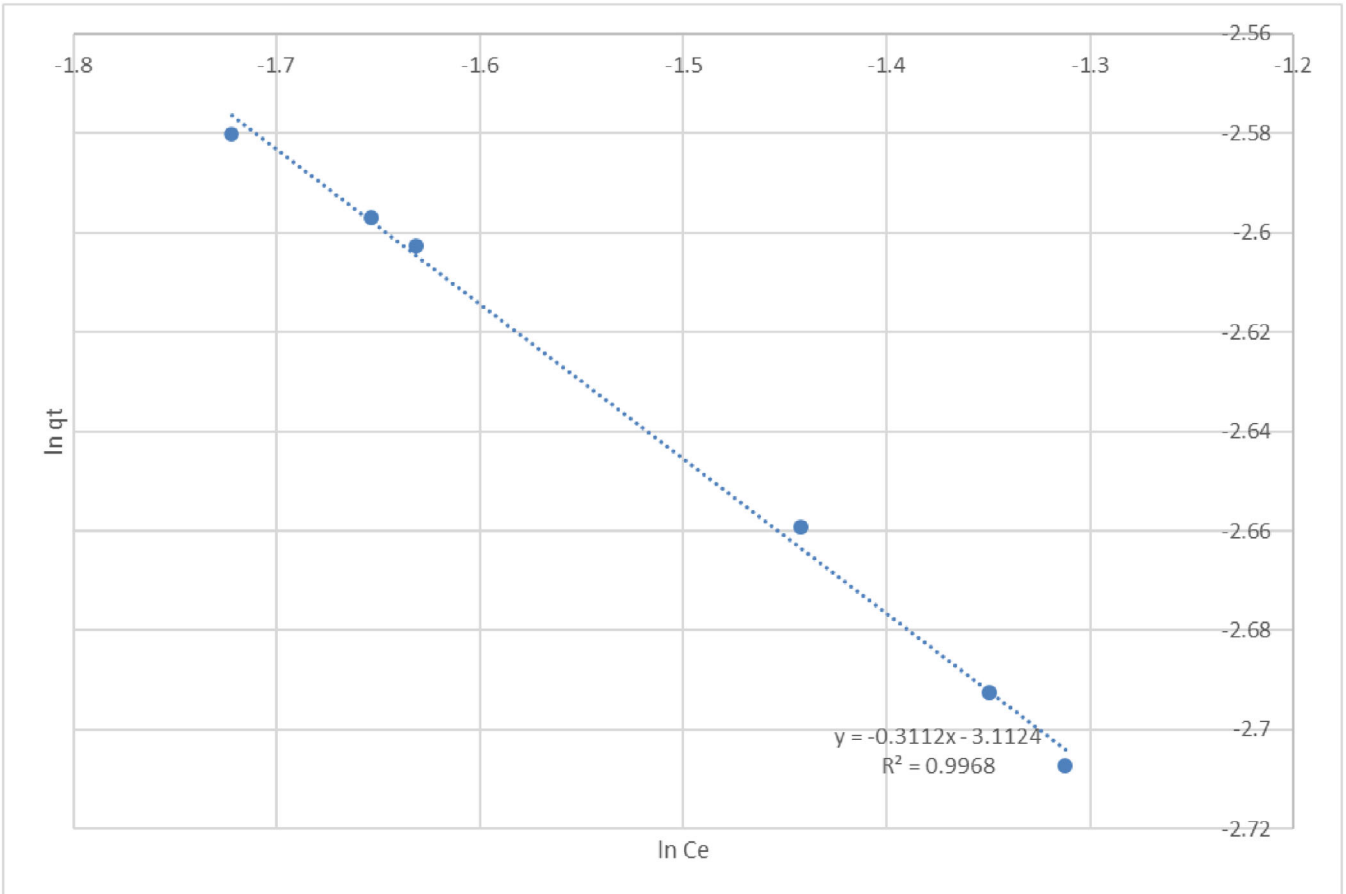

FIGURE 15 | Freundlich isotherm of MIP FA.

TABLE 3 | Kinetic studies of MIP FA.

Kinetic models					
Pseudo-first-order			**Pseudo-second-order**		
q_{e1}	K_1	R^2	q_{e2}	K_2	R^2
0.0089	0.004606	0.9506	0.0646	2.0516	0.998

TABLE 4 | Kinetic isotherm of MIP FA.

Kinetic isotherm							
Langmuir isotherm				**Freundlich isotherm**			
q_{max}	K_L	R_L	R^2	K_F	n	$1/n$	R^2
0.0540	19.0323	0.0531	0.9993	0.7325	−3.2134	−0.3112	0.9968

hippuric acid), hormones (estrogens, androgens), metabolites from drug metabolism, plant-derived phenolics, microorganisms and their metabolic byproducts, and numerous other trace organic compounds [39]. The ionic strength of urine (typically 300–400 mOsm/kg) is substantially higher than pure aqueous solutions, creating competition for binding sites on sorbent materials and potentially interfering with molecular recognition mechanisms [40].

This indicates that complexity makes urine a suitable matrix for studying MIP. MIP techniques have an extraordinary potential to be used as a clinical method for analysis of specific components [41].

The application of MIP FA to adsorb 10 μg/mL of FA in urine showed a successful rate of adsorption compared to NIP which is 85.2% and 6.64%, respectively (Table 5). The adsorption is

TABLE 5 | Result of application on MIP FA in urine.

		MIP			NIP		
Samples	**Amount of FA added (μg/mL)**	**Amount of FA found (μg/mL)**	**Recovery (%)**	**RSD**	**Amount of FA found (μg/mL)**	**Recovery (%)**	**RSD**
Urine	10	8.52	85.2	0.05	0.664	6.64	0.12

also supported by the RSD value which shows the precision in methodology. To fully appreciate this result, it is essential to understand the mechanisms by which urine complexity normally challenges extraction methods, and how the nano-sized molecularly imprinted polymers (nanoMIP) successfully navigates these challenges. The template-imprinted cavities are geometrically and chemically complementary to FA specifically, providing binding affinity and selectivity that nonspecific competitors cannot match [3].

These results showing that MIP have high selectivity, affinity and sensitivity to detect and adsorp FA in urine (ADD MORE POINT). The recovery of template from spiked samples with different concentrations was sufficiently acceptable, demonstrating the reliable, selective, and accurate performance of the synthesized MIP in cleaning up complex samples [42].

Molecular imprinting is widely acknowledged for its remarkable capability to create custom-designed recognition sites that preserve the specific attributes of template molecules, including their shape, size, and functional groups. This unique feature allows MIPs to exhibit high selectivity and affinity for target analytes [38].

This molecular-scale selectivity manifested at the imprinted cavity level protects the target molecule from competition by the thousands of structurally related compounds present in urine [12]. These findings establish an effective MIP-based solid-phase extraction (SPE) method for FA sample preparation with potential applications in analytical sample cleanup prior to chromatographic quantification, environmental remediation, and food extract purification.

3 | Methods

3.1 | Preparation of Microemulsion Solvent

The porogen solvent used in this research was listed in Table 1. To determine the appropriate amount utilized for the polymerization process, some calculations had been made (Table 6).

3.2 | Synthesis of MIP and NIP

The MIP was synthesized by dissolving 1 mmol of FA in 100 mL of microemulsion solvent and transferring the mixture into a 250 mL conical flask. Subsequently, 4 mmol of MAA as the functional monomer, 8 mmol of ethylene glycol dimethacrylate (EGDMA) as the crosslinker, and 0.030 g of benzoyl peroxide blended with dicyclohexyl phthalate as the radical initiator were added. The resulting solution was sonicated for 10 min to enhance dispersion and degassed by purging with nitrogen gas for 15 min to eliminate dissolved oxygen. The flask was then sealed and subjected to thermal polymerization in a water bath at 80°C for 6 h. A NIP was prepared under identical conditions in the absence of FA. Post-polymerization, the MIP was thoroughly washed with a methanol–acetic acid mixture (60:40 *v*/*v*) until complete removal of the template molecule was confirmed.

TABLE 6 | Composition of microemulsion.

Chemicals	**Volume (mL)/ amount (g) used**
Sodium dodecyl sulfate (SDS)	8.0 g
Distilled water (H_2O)	160 mL
Hexane	8 mL
Butan-1-ol	25 mL

3.3 | Batch Binding

Adsorption experiments were carried out in a series of 100 mL conical flasks. Each flask contained 10 mL of a 10 ppm FA solution and approximately 0.1 g of either MIP or NIP particles while the pH value of FA solution natural (7) The flasks were placed on an orbital shaker and agitated at 150 rpm. Samples were withdrawn at predetermined time intervals (0, 5, 10, 15, 20, 25, 30, 60, 90, 120, and 150 min). The concentration of FA in each sample was analyzed using UV–vis spectrophotometry at a wavelength of 285 nm.

The binding efficiency (%) of both MIP and NIP was calculated using the following equation:

$$\text{Binding efficiency} = \frac{(C_i - C_f)}{C_i} \times 100 \quad (1)$$

where C_i and C_f represent the initial and final concentrations of FA in the solution, respectively.

3.4 | Kinetic Studies of MIP-FA

PFO, PSO, and intraparticle-diffusion kinetic models were tested in kinetic study to differentiate the FA adsorption process on the MIP FA surface. Investigating the kinetics of adsorption proved to be a valuable method for analyzing both the rate of adsorption and the basic principle of sorption.

Out of all the kinetic models considered, only one model which demonstrates a higher correlation coefficient (R^2) should be

TABLE 7 | Linear form and plot for kinetic studies.

Kinetic study	Pseudo-first-order	Pseudo-second-order
Linear form	$loglog\,(q_e - q_t) = loglog\,(q_e) - K_1(\frac{t}{2.303})$	$\frac{t}{q_t} = \frac{1}{K_2(q_e)^2} + \frac{t}{q_e}$
Plot	$loglog\,(q_e - q_t)\ against\ t$	$\frac{t}{q_t}\ against\ t$

Abbreviations: K_1, the PFO equilibrium rate constant; K_2, the PSO equilibrium rate constant, K_{diff}, the intraparticle equilibrium rate constant; q_e, the amount of FA adsorbed at equilibrium; q_t, the amount of FA adsorbed at any given time; C, another Kinetic constant; t, the time interval of FA adsorption.

TABLE 8 | Linear form and plot for adsorption isotherm.

Adsoprtion isotherm	Langmuir	Freundlich
Linear form	$\frac{C_e}{q_e} = (\frac{1}{q_{max}KL}) + (\frac{C_e}{q_{max}})$	$ln\,(q_e) = lnln\,(K_F) + \frac{1}{n} ln\,C_e$
Plot	$(\frac{C_e}{q_e}) against\ C_e$	$ln\,(q_e)\ \ against\,(C_e)$

Abbreviations: q_e, the amount of FA adsorbed at equilibrium; q_t, the amount of FA adsorbed at any given time.

chosen as the most accurate model for describing the adsorption of MIP FA.

The linear equation in Table 7 designated the PFO, PSO, and, respectively [17].

The amount of FA adsorbed at equilibrium (q_e) and the amount of FA adsorbed at any given time (q_t) will be calculated with the equation below:

$$q_e = \frac{V}{m}(C_i - C_e) \tag{2}$$

$$q_t = \frac{V}{m}(C_i - C_t) \tag{3}$$

Equation of amount of FA adsorbed at equilibrium (q_e) and the amount of FA adsorbed at any given time (q_t), C_i, initial concentration of FA; C_e, final concentration of FA at equilibrium; C_t, final concentration of FA at given time; V, volume of FA solution; m, mass of MIP-FA.

3.5 | Adsorption Isotherms of MIP-FA

This study applied three isotherm models, mainly Langmuir Isotherm, Freundlich Isotherm, and Temkin Isotherm to characterize the adsorption capacity and surface properties of the MIP-FA. Out of these three isotherm models, only one model will be chosen as the best-fitted isotherm model based on the higher correlation coefficient (R^2) [18]. The linear equations in Table 8 are designated for Langmuir and Freundlich, respectively [17].

Moreover, the values of RL (parameter of equilibrium) related to the fundamental characteristics of the Langmuir model were computed by applying:

$$R_L = \frac{1}{1 + K_L C_o} \tag{4}$$

where K_L is the Langmuir constant and C_o is the highest FA initial concentration.

3.6 | Adsorption Test

3.6.1 | Initial Concentration

A series of FA solutions were prepared at concentrations of 0, 5, 10, 15, 25, and 30 ppm by dissolving the FA template in a methanol (MeOH) and deionized water (DIW) mixture with a volume ratio of 1:9 (*v*/*v*). To evaluate the rebinding capacity, 0.1 g of MIP beads and NIP beads were individually introduced into separate 100 mL conical flasks, each containing 10 mL of the respective FA solution. These mixtures were then subjected to agitation on an orbital shaker at 150 rpm for 30 min and pH of FA solution is neutral (7) ensuring adequate interaction between the polymers and FA molecules. The rebinding efficiency for both MIP and NIP beads was determined with Equation (1).

3.6.2 | Polymer Dosage

A series of 100 mL conical flasks were each filled with 10 mL of FA solution at a concentration of 10 ppm, prepared by dissolving the FA template in a methanol (MeOH) and DIW mixture at a 1:9 (*v*/*v*) ratio, with the pH adjusted to 7. Different amounts of MIP and NIP beads 0.1, 0.2, 0.3, 0.4, 0.5, and 0.6 g were added separately to the flasks. The mixtures were agitated on an orbital shaker at 150 rpm for 30 min to promote the rebinding of FA to the beads. After incubation, the remaining FA concentrations in the solutions were measured using a UV–vis spectrophotometer. The rebinding efficiency of the MIP and NIP beads for FA was calculated using the following Equation (1).

3.6.3 | pH

A fixed amount of 0.1 g of MIP and NIP beads were individually added to a series of 100 mL conical flasks containing 10 mL of

FA solution at a concentration of 10 ppm. The FA solution was prepared in a methanol (MeOH) and DIW mixture with a volume ratio of 1:9 (*v*/*v*), and the pH was adjusted to values of 3, 5, 7, 9, and 11. The mixtures were agitated on an orbital shaker at 150 rpm for 30 min to promote rebinding of FA onto the polymer beads. Following the incubation period, the residual FA concentrations were determined using a UV–vis spectrophotometer. Rebinding efficiencies of both MIP and NIP beads across the various pH levels were subsequently calculated according to Equation (1).

3.7 | Selectivity Test

In this study Riboflavin was used as the competitive template. In two different flasks, equal volumes (10 mL) and concentrations (10.0 ppm) of both templates were combined together and treated with MIP and NIP (0.1 g). After that, both flasks were shaken for 30 min at 150 rpm on a shaker. FA and Riboflavin concentrations were measured using UV–vis Spectrophotometer. The distribution coefficient was calculated by the following Equation (4).

$$KD = \left[\frac{(C_i - C_f)}{C_f}\right]\left[\left(\frac{V}{m}\right)\right] \quad (5)$$

where K_D is the distribution coefficient, C_i and C_f are the initial and final solution concentrations, and V and M are the volume of solution and mass of MIP or NIP utilized, respectively.

The selectivity coefficients (K) for FA in comparison to binding competitor for MIP and NIP were calculated by using following equation:

$$\text{Selectivity coefficient, } K = \left[\frac{K_D^{FA}}{K_D^{RB}}\right] \quad (6)$$

The distribution coefficients of FA acid and are denoted as K_D^{FA} and K_D^{RB}, respectively.

As a result, the relative selectivity coefficient (K') was calculated using the following equation:

$$K' = \frac{K_{MIP}}{K_{NIP}} \quad (7)$$

3.8 | Application

Approximately 100 mL of freshly obtained, drug-free human urine was centrifuged and filtered. The resulting supernatant was spiked with FA to a final concentration of 10 ppm, and a 50 mL portion of this spiked sample was added to a flask containing 0.1 g of FA-imprinted MIP. The sample was then processed according to the previously described batch binding assay, with the NIP undergoing identical treatment.

4 | Conclusion

This study successfully developed nanoMIPs for selective FA extraction, achieving comprehensive performance optimization and validation. The nanoMIP exhibited a mean particle diameter of 42.72 nm (vs. 83.17 nm for NIP controls), providing 20-fold higher surface area (106.44 m^2/g vs. 5.35 m^2/g) and shortened diffusion pathways enabling rapid equilibration.

Under optimized conditions (pH 7.0, 0.1 g dosage, 30 min contact time, 10 ppm FA), the nanoMIP achieved 80.92% binding efficiency with 1.38-fold enhancement over NIP controls. pH profiling (pH 1–13) confirmed binding specificity, with efficiency collapsing at extreme pH (3.85% at pH 1, 4.74% at pH 13). Time-dependent kinetics demonstrated equilibrium within 30 min with PSO kinetic modeling ($R^2 = 0.9986$) confirming surface-reaction-limited binding. Selectivity studies using riboflavin competitor showed relative selectivity coefficient of 1.12, demonstrating preferential template recognition.

When applied to spiked human urine samples, the nanoMIP achieved 85.2% FA recovery at physiological pH, requiring no sample pre-treatment, which is a significant advantage for clinical diagnostics.

This comprehensive characterization demonstrates that the nanoMIP platform successfully overcomes limitations of conventional bulk-MIP approaches through nano-scale efficiency (42.72 nm, 20× surface area), optimized binding conditions (pH 7, rapid 30-min equilibration), confirmed selectivity (1.38-fold vs. NIP), and proven clinical applicability (85.2% urine recovery). These results establish a robust extraction system with potential applications in clinical diagnostics, environmental remediation, and food analysis remediation.

Author Contributions

A.F.M.R. conducted the experimental work, data analysis, and drafted the article. R.M.R. and S.A.B. supervised the research, provided conceptual guidance, and reviewed the article. M.S.S. and A.F.S. provided additional supervision and article review. All authors approved the final version.

Funding

This research was supported by the Universiti Malaysia Sarawak (UNIMAS) under grant number F07/PARTNERS/2115/2021.

Data Availability Statement

The data that support the findings of this study are available from the corresponding author upon reasonable request.

References

1. Z. Wang, R. Long, M. Peng, T. Li, and S. Shi, "Molecularly Imprinted Polymers-Coated CdTe Quantum Dots for Highly Sensitive and Selective Fluorescent Determination of Ferulic Acid," *Journal of Analytical Methods in Chemistry* 2019 (2019): 1, https://doi.org/10.1155/2019/1505878.

2. A. Rauf, R. Ajaj, Z. Akram, et al., "Ferulic Acid as a Promising Candidate for Developing Selective and Effective Anti-Cancer Therapies," *Discover Oncology* 16, no. 1 (2025): 1214, https://doi.org/10.1007/s12672-025-02294-9.

3. M. Mora-Granados, D. González-Gómez, J. S. Jeong, and A. Gallego-Picó, "A Molecularly Imprinted Polymer for Selective Extraction of Phenolic Acids From Human Urine," *Applied Sciences* 11, no. 4 (2021): 1577, https://doi.org/10.3390/app11041577.

4. S. A. Bhawani, A. F. M. Ramezan, R. M. Roland, M. A. Othman, and A. F. Simbas, "Synthesis of Molecularly Imprinted Polymers for the Extraction of p-Hydroxybenzoic Acid," *Asian Journal of Chemistry* 37, no. 7 (2025): 1736–1742, https://doi.org/10.14233/ajchem.2025.33574.

5. S. R. Shafqat, S. A. Bhawani, S. Bakhtiar, M. N. M. Ibrahim, and S. S. Shafqat, "Template-Assisted Synthesis of Molecularly Imprinted Polymers for the Removal of Methyl Red From Aqueous media," *BMC Chemistry* 17, no. 1 (2023): 46, https://doi.org/10.1186/s13065-023-00957-8.

6. O. I. Parisi, F. Francomano, and M. Dattilo, et al., "The Evolution of Molecular Recognition: From Antibodies to Molecularly Imprinted Polymers (MIPs) as Artificial Counterpart," *Journal of Functional Biomaterials* 13, no. 1 (2022): 12, https://doi.org/10.3390/jfb13010012.

7. M. Gao, Y. Gao, G. Chen, et al., "Recent Advances and Future Trends in the Detection of Contaminants by Molecularly Imprinted Polymers in Food Samples," *Frontiers in Chemistry* 8 (2020): 616326, https://doi.org/10.3389/fchem.2020.616326.

8. A. Zare, B. Babamiri, M. Hassani, M. Khalghollah, S. H. Javanmard, and A. Sanati-Nezhad, "Mip-Chip: Self-Operating Molecularly Imprinted Polymer (MIP) Biosensor for Point-of-Care Diagnostics," *SSRN Electronic Journal* (2025), 5151209, https://doi.org/10.2139/ssrn.5151209.

9. K. Yoshimatsu, K. Reimhult, A. Krozer, K. Mosbach, K. Sode, and L. Ye, "Uniform Molecularly Imprinted Microspheres and Nanoparticles Prepared by Precipitation Polymerization: The Control of Particle Size Suitable for Different Analytical Applications," *Analytica Chimica Acta* 584 (2007): 112–121, https://doi.org/10.1016/j.aca.2006.11.004.

10. U. Zulfiqar, N. Kostoglou, A. G. Thomas, C. Rebholz, A. Matthews, and D. J. Lewis, "Flexible Nanoporous Activated Carbon for Adsorption of Organics From Industrial Effluents," *Nanoscale* 13, no. 36 (2021): 15311–15323, https://doi.org/10.1039/d1nr03242a.

11. J. J. Max and C. Chapados, "Infrared Spectroscopy of Aqueous Carboxylic Acids: Comparison Between Different Acids and Their Salts," *Journal of Physical Chemistry A* 108, no. 16 (2004): 3324–3337, https://doi.org/10.1021/jp036401t.

12. R. M. Roland, S. A. Bhawani, and M. N. M. Ibrahim, "Synthesis of Molecularly Imprinted Polymer for the Removal of Cyanazine From Aqueous Samples," *Chemical and Biological Technologies in Agriculture* 10, no. 1 (2023): 92, https://doi.org/10.1186/s40538-023-00462-z.

13. R. A. Lorenzo, A. M. Carro, C. Alvarez-Lorenzo, and Á. Concheiro, "To Remove or Not to Remove? The Challenge of Extracting the Template to Make the Cavities Available in Molecularly Imprinted Polymers (MIPs)," *International Journal of Molecular Sciences* 12, no. 7 (2011): 4327–4347, https://doi.org/10.3390/ijms12074327.

14. A. Lamaoui, V. Mani, C. Durmus, K. Saláma, and A. Amine "Molecularly Imprinted Polymers: A Closer Look at the Removal and Rebinding of Templates," (2023), https://doi.org/10.2139/ssrn.4535773.

15. H. Lu, H. Tian, C. Wang, and S. Xu, "Designing and Controlling the Morphology of Spherical Molecularly Imprinted Polymers," *Materials Advances* 1 (2020): 2182–2201, https://doi.org/10.1039/D0MA00415D.

16. R. M. Roland, S. A. Bhawani, M. N. M. Ibrahim, and R. Wahi, "Synthesis and Characterizations of Molecularly Imprinted Polymer of Atrazine: Removal of Atrazine From Aqueous Samples," *ChemistrySelect* 9, no. 1 (2024): e202303679.

17. M. V. Sullivan, C. Fletcher, R. Armitage, C. Blackburn, and N. W. Turner, "A Rapid Synthesis of Molecularly Imprinted Polymer Nanoparticles for the Extraction of Performance Enhancing Drugs (PIEDs)," *Nanoscale Advances* 5, no. 19 (2023): 5352–5360, https://doi.org/10.1039/d3na00422h.

18. A. M. Rosengren, B. Karlsson, and I. A. Nicholls, "Consequences of Morphology on Molecularly Imprinted Polymer-Ligand Recognition," *International Journal of Molecular Sciences* 14, no. 1 (2013): 1207–1217, https://doi.org/10.3390/ijms14011207.

19. M. M. Sanagi, S. Salleh, W. A. W. Ibrahim, and A. A. Naim, "Molecularly Imprinted Polymers for Solid Phase Extraction of Orghanophosphorus Pesticides," *Malaysian Journal of Fundamental and Applied Sciences* 6 (2010): 27–30.

20. J. Chen, L. Bai, K. Liu, R. Liu, and Y. Zhang, "Atrazine Molecular Imprinted Polymers: Comparative Analysis by Far-Infrared and Ultraviolet Induced Polymerization," *International Journal of Molecular Sciences* 15 (2014): 574–587, https://doi.org/10.3390/ijms15010574.

21. H. Men, H. Liu, and Z. Zhang, et al., "Synthesis, Properties and Application Research of Atrazine Fe_3O_4@SiO_2 Magnetic Molecularly Imprinted Polymer," *Environmental Science and Pollution Research* 19 (2012): 2271–2280, https://doi.org/10.1007/s11356-011-0732-9.

22. T. Xolo and P. Mahlambi, "Molecularly Imprinted Polymers as Solid-Phase and Dispersive Solid-Phase Extraction Sorbents in the Extraction of Antiretroviral Drugs in Water: Adsorption, Selectivity and Reusability Studies," *Journal of Analytical Science and Technology* 15, no. 1 (2024): 11, https://doi.org/10.1186/s40543-024-00418-4.

23. J. Azay-Milhau, K. Ferrare, and J. Leroy, et al., "Antihyperglycemic Effect of a Natural Chicoric Acid Extract of Chicory (*Cichorium intybus* L.): A Comparative in Vitro Study With the Effects of Caffeic and Ferulic Acids," *Journal of Ethnopharmacology* 150, no. 2 (2013): 755–760, https://doi.org/10.1016/j.jep.2013.09.046.

24. B. Gao, S. Meng, and L. Zhang, "Designing and Preparation of Ferulic Acid Surface-Imprinted Material and Its Molecular Recognition Characteristics," *RSC Advances* 6, no. 5 (2015): 3986–3996, https://doi.org/10.1039/c5ra21725c.

25. R. M. Roland, S. A. Bhawani, and M. N. M. Ibrahim, "Synthesis of Molecularly Imprinted Polymer by Precipitation Polymerization for the Removal of Ametryn," *BMC Chemistry* 17, no. 1 (2023): 165.

26. Y. Wang, Y. Wang, and H. Liu, "A Novel Fluorescence and SPE Adsorption Nanomaterials of Molecularly Imprinted Polymers Based on Quantum Dot-Grafted Covalent Organic Frameworks for the High Selectivity and Sensitivity Detection of Ferulic Acid," *Nanomaterials* 9, no. 2 (2019): 305.

27. S. A. Bhawani, N. B. Suhaili, R. M. Roland, S. Bakhtiar, K. M. Alotaibi, and M. N. M. Ibrahim, "Template Assisted Synthesis of Molecularly Imprinted Polymer for the Extraction of p-Coumaric Acid," *Asian Journal of Chemistry* 32, no. 9 (2020): 2342–2346, https://doi.org/10.14233/ajchem.2020.22833.

28. S. A. Bhawani, S. Bakhtiar, and S. R. Shafqat, "Synthesis of Molecularly Imprinted Polymers for the Selective Extraction /Removal of 2,4,6-Trichlorophenol," *Open Chemical Engineering Journal* 13, no. 1 (2019): 122–133, https://doi.org/10.2174/1874123101912010122.

29. C. Dai, J. Zhang, Y. Zhang, X. Zhou, and S. Liu, "Application of Molecularly Imprinted Polymers to Selective Removal of Clofibric Acid From Water," *PLoS ONE* 8, no. 10 (2013): e78167, https://doi.org/10.1371/journal.pone.0078167.

30. K. Abdollahi, C. Ince, L. Condict, A. Hung, and S. Kasapis, "Combined Spectroscopic and Molecular Docking Study on the pH Dependence of Molecular Interactions Between β-Lactoglobulin and Ferulic Acid," *Food Hydrocolloids* 101 (2019): 105461, https://doi.org/10.1016/j.foodhyd.2019.105461.

31. N. A. Yusof, A. Beyan, M. J. Haron, and N. A. Ibrahim, "Synthesis and Characterization of a Molecularly Imprinted Polymer for PB2+ Uptake Using 2-vinylpyridine as the Complexing monomer," *Sains Malaysiana* 39 (2010): 829–835.

32. A. D. Khatibi, A. H. Mahvi, N. Mengelizadeh, and D. Balarak, "Adsorption–Desorption of Tetracycline Onto Molecularly Imprinted Polymer: Isotherm, Kinetics, and Thermodynamics Studies," *Desalination and Water Treatment* 230 (2021): 240–251, https://doi.org/10.5004/dwt.2021.27396.

33. E. Janus, L. R. Pinheiro, and A. Nowak, et al., "New Ferulic Acid and Amino Acid Derivatives With Increased Cosmeceutical and Pharmaceutical Potential," *Pharmaceutics* 15, no. 1 (2022): 117, https://doi.org/10.3390/pharmaceutics15010117.

34. E. D. Revellame, D. L. Fortela, W. Sharp, R. Hernandez, and M. E. Zappi, "Adsorption Kinetic Modeling Using Pseudo-First Order and Pseudo-Second Order Rate Laws: A Review," *Cleaner Engineering and Technology* 1 (2020): 100032, https://doi.org/10.1016/j.clet.2020.100032.

35. G. Becskereki, G. Horvai, and B. Tóth, "The Selectivity of Molecularly Imprinted Polymers," *Polymers* 13, no. 11 (2021): 1781, https://doi.org/10.3390/polym13111781.

36. Ş. K. Ersoy, E. Tütem, K. S. Başkan, and R. Apak, "Preparation and Application of Caffeic Acid Imprinted Polymer," *Turkish Journal of Chemistry* 47, no. 4 (2023): 699–714, https://doi.org/10.55730/1300-0527.3572.

37. A. A. Sangoremi, "Adsorption Kinetic Models and Their Applications: A Critical Review," *International Journal of Research and Scientific Innovation* XII (2025): 245–258, https://doi.org/10.51244/ijrsi.2025.120500019.

38. R. Vitek and J. C. Masini, "Nonlinear Regression for Treating Adsorption Isotherm Data to Characterize New Sorbents: Advantages Over Linearization Demonstrated With Simulated and Experimental Data," *Heliyon* 9, no. 4 (2023): e15128, https://doi.org/10.1016/j.heliyon.2023.e15128.

39. J. Xu, S. Zheng, M. Li, et al., "A Comprehensive 2D-LC/MS/MS Profile of the Normal Human Urinary Metabolome," *Diagnostics* 12, no. 9 (2022): 2184, https://doi.org/10.3390/diagnostics12092184.

40. S. Leulmi, T. Vemulkar, J. Verheyen, et al., "Lithographically Defined Encoded Magnetic Heterostructures for the Targeted Screening of Kidney Cancer," *Nanoscale Advances* 6, no. 1 (2023): 276–286, https://doi.org/10.1039/d3na00701d.

41. H. A. Mulder, A. C. Pearcy, M. S. Halquist, et al., "Characterization of Molecularly Imprinted Polymers for the Extraction of Tobacco Alkaloids and Their Metabolites in human Urine," *Biomedical Chromatography* 36, no. 6 (2022): e5361, https://doi.org/10.1002/bmc.5361.

42. A. E. E. Amr, A. H. Kamel, A. A. Almehizia, A. Y. A. Sayed, and H. S. M. Abd-Rabboh, "Solid-Contact Potentiometric Sensors Based on Main-Tailored Bio-Mimics for Trace Detection of Harmine Hallucinogen in Urine Specimens," *Molecules* 26, no. 2 (2021): 324, https://doi.org/10.3390/molecules26020324.